



# Electrochemical upgrade of CO<sub>2</sub> from amine capture solution

Geonhui Lee<sup>1,3</sup>, Yuguang C. Li<sup>1,3</sup>, Ji-Yong Kim<sup>2</sup>, Tao Peng<sup>1</sup>, Dae-Hyun Nam<sup>1</sup>,  
Armin Sedighian Rasouli<sup>1</sup>, Fengwang Li<sup>1</sup>, Mingchuan Luo<sup>1</sup>, Alexander H. Ip<sup>1</sup>, Young-Chang Joo<sup>1,2</sup>  
and Edward H. Sargent<sup>1</sup>✉

**CO<sub>2</sub> capture technologies based on chemisorption present the potential to lower net emissions of CO<sub>2</sub> into the atmosphere. The electrochemical upgrade of captured CO<sub>2</sub> to value-added products would be particularly convenient. Here we find that this goal is curtailed when the adduct of the capture molecule with CO<sub>2</sub> fails to place the CO<sub>2</sub> sufficiently close to the site of the heterogeneous reaction. We investigate tailoring the electrochemical double layer to achieve the valorization of chemisorbed CO<sub>2</sub> in an aqueous monoethanolamine electrolyte. We reveal, using electrochemical studies and in situ surface-enhanced Raman spectroscopy, that a smaller double layer distance correlates with improved activity for CO<sub>2</sub> to CO from amine solutions. With the aid of an alkali cation and accelerated mass transport by system design—temperature and concentration—we demonstrate amine-CO<sub>2</sub> conversion to CO with 72% Faradaic efficiency at 50 mA cm<sup>-2</sup>.**

Amine-based chemical solvents capture CO<sub>2</sub> at a point source and convert it into chemisorbed form. Pure CO<sub>2</sub> gas can then be generated from the capture solution by heating the solution to 120–150 °C (refs. 1–3). The subsequent electrochemical upgrade of this CO<sub>2</sub> to value-added products, such as fuels and chemical feedstocks, requires additional energy inputs and processing.

A direct approach to electrochemically convert the chemisorbed CO<sub>2</sub> in the capture solution into reduced chemical products could be powered using renewable energy, and could simplify the process flow.

Amine solutions capture CO<sub>2</sub> via the reaction,



where the nucleophilic N and electrophilic carbon form a bond.

Several factors are necessary for the direct valorization of CO<sub>2</sub> in the RNHCOO<sup>-</sup> via electrochemical reduction. First, the electrical energy required to break the N–C bond will scale proportionately with the strength of the CO<sub>2</sub> binding to the amine solution<sup>4</sup>. Thus, the choice of the amine electrolyte will affect the overpotential of the electrocatalytic reactions. Second, the concentration as well as the diffusivity of RNHCOO<sup>-</sup> will affect mass transport of the reactants. A low concentration of the amine solution leads to competing reactions such as the hydrogen evolution reaction. Finally, since heterogeneous electron transfer is an inner sphere reaction<sup>5</sup>, the distance between RNHCOO<sup>-</sup> and the electrode is expected to play a crucial role in the electrolysis reaction. In order to design an electrochemical system that achieves the direct electrolysis of the amine-CO<sub>2</sub> adduct to value-added products, as well as the electrochemical regeneration of the amine solution, it will be important to choose judiciously the binding strength of the amine, concentration, supporting electrolyte and reaction conditions.

Using an electrochemically generated nucleophile, prior research has achieved CO<sub>2</sub> capture and its subsequently controlled release using quinone<sup>6,7</sup>, bipyridine<sup>8</sup>, thiolate<sup>9</sup> molecules and transition

metal complexes<sup>10</sup>. CO<sub>2</sub> desorption from amine capture solutions has also been achieved using an electrochemically generated redox mediator<sup>11,12</sup>. CO<sub>2</sub> electrolysis in aqueous monoethanolamine (MEA) solution was reported by Chen et al., where the authors provided that the carbamate (MEACOO<sup>-</sup>) and ethanolammonium (MEA<sup>+</sup>) ions serve as the supporting electrolyte, but the carbon source is the dissolved CO<sub>2</sub> (ref. 13). Khurram et al. reported the direct electrolysis of amine-CO<sub>2</sub> to carbonate salts on a non-aqueous electrolyte<sup>14</sup>. They also reported, in an ensuing study, the influence of the different cation salts on the speciation of the amine-CO<sub>2</sub> adduct, and the change in the electrochemical rates due to the different species in the electrolyte<sup>15</sup>.

Yet, even with these major studies, the field has yet to report electrolysis to higher value products from the amine-CO<sub>2</sub> adduct at greater than 50 mA cm<sup>-2</sup> operating current densities with high conversion efficiency to CO.

Here we report the direct electrolysis of the chemisorbed amine-CO<sub>2</sub> by tailoring the electrochemical double layer (EDL) using alkali cations. When we introduce alkali cations in amine-CO<sub>2</sub> electrolyte, these alter the composition of the EDL in a way that facilitates the heterogeneous electron transfer to carbamate, a finding we elaborate on using electrochemical impedance spectroscopy (EIS) and in situ surface-enhanced Raman spectroscopy. Under optimized conditions, we achieve a 72% Faradaic efficiency (FE) of CO<sub>2</sub> to CO at an applied current density of 50 mA cm<sup>-2</sup>. We demonstrate the successful recycling of the amine electrolyte with consistent CO FE over the course of multiple cycles of capture–electrolysis.

## The EDL in amine-CO<sub>2</sub> systems

From a system design perspective, CO<sub>2</sub> can be released from amine capture solution via in-situ-generated H<sup>+</sup> from a bipolar membrane to achieve direct electrolysis<sup>16</sup>. We demonstrate this concept with a 30 wt% aqueous MEA electrolyte at different applied current densities ranging from 50–200 mA cm<sup>-2</sup> (Supplementary Fig. 1). The MEA electrolyte is first purged with CO<sub>2</sub> to form the MEA-CO<sub>2</sub>

<sup>1</sup>Department of Electrical and Computer Engineering, University of Toronto, Toronto, Ontario, Canada. <sup>2</sup>Department of Materials Science and Engineering, Seoul National University, Seoul, Republic of Korea. <sup>3</sup>These authors contributed equally: Geonhui Lee, Yuguang C. Li ✉e-mail: [ted.sargent@utoronto.ca](mailto:ted.sargent@utoronto.ca)

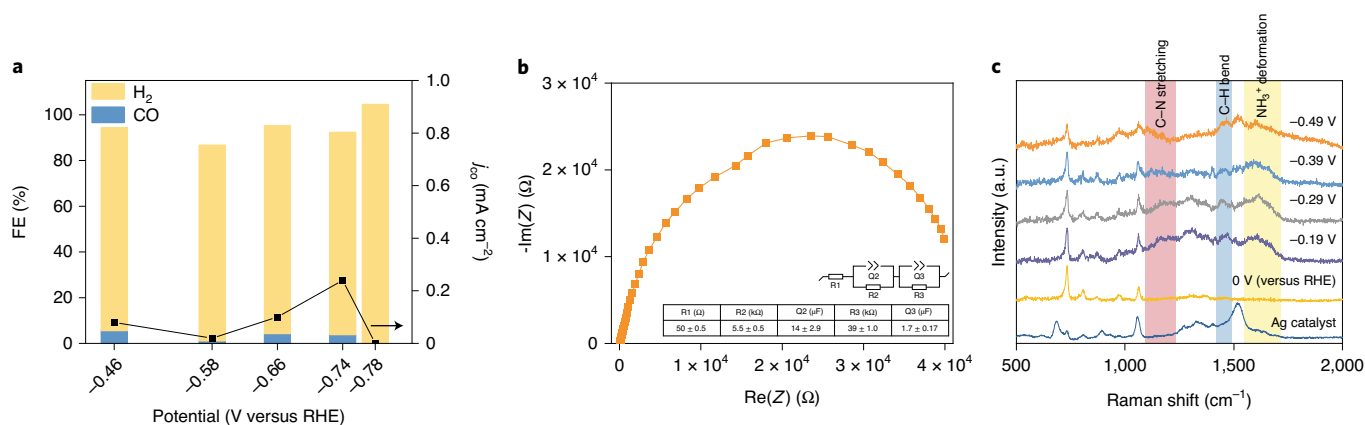


**Fig. 1 | The EDL in the case of MEA electrolyte.** **a**, FE and partial current density ( $j$ ) of CO for the 2 M MEA electrolyte with a Ag electrocatalyst. **b**, Impedance spectra for the 2 M MEA collected at open circuit potential, approximately  $-0.15$  V versus Ag/AgCl. The inset is the equivalent circuit and the fit values of each of the components. Q2 and Q3 are the constant phase element; R1 is the series resistance; R2 and R3 are the charge transfer resistances. The error of each component denotes the standard deviation of three fit values from independent measurements. Z, impedance. **c**, In situ surface-enhanced Raman spectroscopy for the 2 M MEA electrolyte.

adduct, and then purged with N<sub>2</sub> to remove dissolved CO<sub>2</sub> to exclude the possibility of its reduction. The CO FE is below 5% at all current densities tested and for the amine–CO<sub>2</sub> electrolytes studied (MEA–CO<sub>2</sub>, diethanolamine–CO<sub>2</sub> and *N*-methyldiethanolamine–CO<sub>2</sub>). The low FE is due to the utilization rate of the in-situ-generated CO<sub>2</sub>; unreacted CO<sub>2</sub> returns to the MEA–CO<sub>2</sub> adduct, and the local concentration of CO<sub>2</sub> on the surface of the catalyst is not high enough.

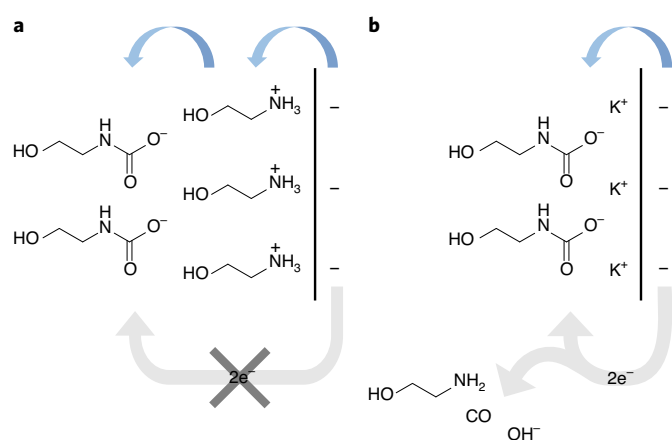
The direct electrolysis of the MEA–CO<sub>2</sub> offers an approach that circumvents the limitation of the low solubility of CO<sub>2</sub>. We pursued direct electrolysis using a Ag electrocatalyst as the cathode in an amine–CO<sub>2</sub> electrolyte. The Ag electrocatalyst is prepared according to the procedures noted under catalyst preparation in the Methods section and is characterized by scanning electron microscopy, X-ray photoelectron spectroscopy and X-ray diffraction to reveal the morphology and surface composition (Supplementary Figs. 2–4). We studied both three-electrode systems and flow cell systems. Pt foil and a 3 M Ag/AgCl electrode were used as the anode electrode and reference electrode, respectively, separated by a Nafion membrane for ion migration. The catholyte in all studies was purged with CO<sub>2</sub> to form MEA–CO<sub>2</sub>, after which N<sub>2</sub> was used for purging for a minimum of 20 min to remove dissolved CO<sub>2</sub> (Supplementary Table 6) to confirm that MEA–CO<sub>2</sub> is a reactant. Upon absorption of the CO<sub>2</sub> molecule, MEA turns into ethanolammonium ion and carbamate<sup>13</sup>, and these serve as the supporting electrolyte and the reactant. All potentials in this study are referenced to the reversible hydrogen electrode (RHE) scale unless otherwise noted.

Figure 1a shows the FE of a 2 M MEA-only electrolyte; the CO FE values are below 5% for all the potentials tested. We posited that the low FE arises due to the inefficiency of electron transfer between the electrode and the carbamate molecule. We conducted EIS and in situ surface-enhanced Raman spectroscopy to investigate electron transfer between the surface and species in the EDL.

EIS spectra (Fig. 1b) for the MEA electrolyte under open circuit conditions have two distinct semicircles, indicating two charge transfer processes. The equivalent circuit shown in the inset of Fig. 1b is fit using two interfacial charge transfer resistances (R2 and R3), each coupled with a double layer capacitance (Q2 and Q3, which are also known as constant phase elements). In light of the frequency range tested herein from 10<sup>5</sup> Hz to 0.01 Hz, the equivalent circuit represents only charge transfer processes, and not a diffusion-limited process. The corresponding fits of the capacitance for each of the semicircles differ by 14 μF and 1.7 μF, consistent

with two distinct charge transfer processes. The two processes are observed in the frequency range 10 Hz to 100 Hz and 1 Hz to 0.1 Hz. Each frequency range is consistent with the timescale of a charge transfer reaction<sup>17</sup>. In the MEA electrolyte, ethanolammonium and carbamate are the only ionic species capable of forming the EDL. Thus, the cationic ethanolammonium ion should occupy the inner Helmholtz layer, and the high frequency arc of the EIS spectra corresponds to the EDL charging action of the ethanolammonium ion. The low frequency arc of the EIS spectra corresponds to charge transfer to the carbamate molecule—the reaction step. Since H<sub>2</sub> is an observed reaction product, the low frequency arc of the EIS spectra could also correspond to the charge transfer process to H<sub>2</sub>O. Nonetheless, Fig. 1b shows the ethanolammonium ion in the EDL and a charge transfer process corresponding to charge transfer from the inner Helmholtz layer to the outer Helmholtz layer<sup>18–20</sup>. We conducted EIS measurements under negative polarization to examine further the EDL structure at the interface (Supplementary Fig. 5). The EIS spectra show similar behaviour to the open circuit potential condition: for the MEA electrolyte there are two semicircles indicating two interfacial structures. The result suggests the cationic ethanolammonium ion forms the inner Helmholtz layer due to the negatively biased surface, and two different electron transfers occur.

To probe further the electrode–electrolyte interface, we performed in situ surface-enhanced Raman spectroscopy to investigate the surface species under different applied potentials. In light of the complex molecular system with Nafion binder, MEA, ethanolammonium ion and carbamate molecules, we extracted the amine–CO<sub>2</sub> adduct spectrum by first identifying the peaks from the Nafion binder. Figure 1c (Supplementary Fig. 6 for a zoomed-in version) shows the Raman spectra at different potentials. The Ag catalyst spectrum corresponds to the catalyst with Nafion binding without electrolyte. The Nafion molecular vibrations span 600 cm<sup>-1</sup> to 1,600 cm<sup>-1</sup>; thus, reaction intermediate species in this region are not considered<sup>21,22</sup>. In the region where the Nafion peaks are absent, we assign the spectrum appearing between 1,100 cm<sup>-1</sup> to 1,200 cm<sup>-1</sup> to the C–N stretching mode of the ethanolammonium ion in the electrolyte<sup>23–26</sup>. The peak at 1,604 cm<sup>-1</sup> is assigned to the deformation mode of the ammonium cation (NH<sub>3</sub><sup>+</sup>) in the ethanolammonium ion on the Ag surface<sup>27–29</sup>. The signal broadens and diminishes beyond  $-0.49$  V (versus RHE) as a result of the H<sub>2</sub> gas bubbles. The spectroscopic results suggest the adsorption of an organocation on the electrode surface.



**Fig. 2 | Proposed interfacial structure near the electrode surface.** **a**, MEA- $\text{CO}_2$  electrolyte. **b**, MEA- $\text{CO}_2$  with alkali salt electrolyte.

Taken together, the EIS and in situ Raman studies suggest an interfacial electron transfer mechanism, illustrated in Fig. 2a. In the pure MEA electrolyte, as ethanolammonium is the sole cation in the electrolyte, it forms the primary EDL under negative bias conditions. The orientation or the conformation of the EDL may vary under different negative bias conditions; yet even so, electron transfer must first go through the ethanolammonium before reaching carbamate due to the length of the molecular chain—consistent with observations in the EIS spectra.

These observations motivated us to study the composition of the EDL and its effect on electron transfer dynamics. Theoretical and experimental studies have proposed means by which the activity and selectivity of the  $\text{CO}_2$  reduction reaction and the oxygen reduction reaction are affected by the adsorbates in the Helmholtz layer<sup>15,30–33</sup>; the adsorbates influence the reaction dynamics by positioning the reactants relative to the interface<sup>30,34–37</sup>. These studies show that the steric properties of the adsorbates represent a factor that variously hinders or promotes the interaction of surface species with the catalyst.

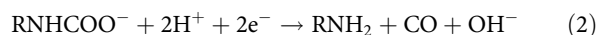
Systematic tuning of the EDL, through the introduction of properly sized electrolyte ions, therefore has the potential to provide an added degree of freedom to disrupt the undesired charge-blocking layer and achieve electron transfer to carbamate, and thus direct electrolysis.

Figure 2b presents an electrochemical system designed for the direct electrochemical conversion of amine- $\text{CO}_2$  with the aid of alkali cations.

Beginning with potassium, we show (Fig. 3a) the product distribution of amine- $\text{CO}_2$  electrolysis for an electrolyte of 2 M MEA with 2 M KCl. It exhibits improved  $\text{CO}_2$  reduction reaction FE compared to pure MEA electrolyte (Fig. 1a), suggesting that the direct conversion of amine- $\text{CO}_2$  to CO was improved upon the introduction of the cation. We also demonstrated electrochemical performance with different ratios of supporting electrolyte from 0.1 M to 3 M (Supplementary Fig. 7). Using isotopically labelled  $^{13}\text{CO}_2$  (Supplementary Fig. 8), we determined that the products observed in these reactions come from  $\text{CO}_2$  captured by MEA. The isotope studies ruled out any chemical decomposition that could lead to false product detection. We investigated possible substrate effects by conducting control experiments with a carbon electrode, in which we found that carbon-based electrocatalysts produced only  $\text{H}_2$  and did so only at a background level of current density  $\sim 100 \mu\text{A}$  (Supplementary Fig. 9). In Fig. 3b, the EIS spectra of the MEA/KCl electrolyte show only one semicircle feature throughout the frequency

range tested. Thus, the equivalent circuit shown in the inset of Fig. 3b is fit as a charge transfer process coupled with R2 (charge transfer resistance) and Q2 (the constant phase element). The EIS spectra indicates an interfacial structure that is distinct from that of the pure MEA electrolyte. The Raman spectra acquired with the MEA/KCl electrolyte (Fig. 3c and Supplementary Fig. 6b) show that the peak features between  $1,100 \text{ cm}^{-1}$  and  $1,700 \text{ cm}^{-1}$ , corresponding to the MEA, ethanolammonium ion and carbamate molecules, have substantially disappeared, suggesting that ethanolammonium ion is no longer the dominant surface species. The surface EDL capacitances for a MEA versus MEA/KCl electrolyte (Supplementary Fig. 10) show that use of the  $\text{K}^+$  ion leads to a more compact double layer on the electrode surface compared to the case of ethanolammonium cation, in agreement with the view that the molecular size of the ethanolammonium cation is larger than that of the hydrated  $\text{K}^+$  in the EDL.

Taken together, the electrochemical and spectroscopic studies suggest that in pure MEA, the ethanolammonium ion is the only cationic species in the electrolyte, and thus forms a monolayer on the reducing electrode surface, accounting for the sharp molecular features in the Raman spectra (Fig. 1c). For the MEA/KCl electrolyte, the  $\text{K}^+$  ion competes for surface binding sites and replaces the ethanolammonium ion. The direct electrochemical conversion of amine- $\text{CO}_2$  based on tailoring the EDL with the aid of a suitably sized cation is then achieved according to equation (2):



### Tailoring the double layer using alkali cations

We further examine different alkali cations ( $\text{Li}^+$ ,  $\text{Na}^+$ ,  $\text{K}^+$ ,  $\text{Rb}^+$  and  $\text{Cs}^+$ ) to gain insight into how the size of the cationic species affects the EDL and the reduction of the MEA- $\text{CO}_2$  adduct. We compare different cation species by adding 2 M of the respective salt to the MEA electrolyte at applied potentials of  $-0.58 \text{ V}$  and  $-0.66 \text{ V}$  versus RHE, shown in Fig. 4a. A wider potential range of the CO FE, from  $-0.46 \text{ V}$  to  $-0.78 \text{ V}$  versus RHE, is shown in Supplementary Fig. 14. The CO FE values for the  $\text{Li}^+$  and  $\text{Na}^+$  electrolyte are similar to those of the 2 M MEA electrolyte, which is below 5%.  $\text{Cs}^+$  electrolyte shows the best performance, with 30% CO FE at  $-0.66 \text{ V}$  versus RHE.  $\text{Cs}^+$  has the smallest hydrated ionic radius, whereas  $\text{Li}^+$  has the largest due to the difference in water coordination<sup>38</sup>. The abrupt changes in CO FE argue against the possibility that, in this work, the cation serves to improve the adsorption energy of reactants by increasing the strength of electric field<sup>33,38</sup>. Prior studies observed a gradual increase in product conversion efficiency as the cationic size increased, whereas herein, the product was not detected in the case of  $\text{MEA}\text{H}^+$ ,  $\text{Li}^+$  and  $\text{Na}^+$ . We also considered a cation effect buffering local pH on the cathode surface to maintain the  $\text{CO}_2$  concentration<sup>39</sup>; however, the reactant in our system is in the molar range, and this is sufficient for reaction without need of buffering. We further examined the effects of different anions in the electrolyte and found that the electrochemical performance was similar for the different anions tested ( $\text{Cl}^-$ ,  $\text{HCO}_3^-$  and  $\text{CH}_3\text{COO}^-$ ; Supplementary Fig. 15). These electrochemical observations are consistent with a picture of the interfacial structure (Fig. 2) wherein the EDL at the cathode consists largely of cationic species, and the anionic species have a minimal effect on electron transfer within the Helmholtz layer. Hydrogen evolution is relatively unaffected by the cation size<sup>33,38</sup>, and thus the differences in the electrochemical performance arise primarily from the change in the interfacial structure<sup>30,37</sup>.

In order to explore further how tailoring the electrochemical layer by cationic species affects the electron transfer, we investigated the interfacial electric field strength via the Stark tuning. The vibration frequency associated with surface intermediates, such as adsorbed CO ( $\text{CO}_{\text{ads}}$ ), depends on the applied potential.

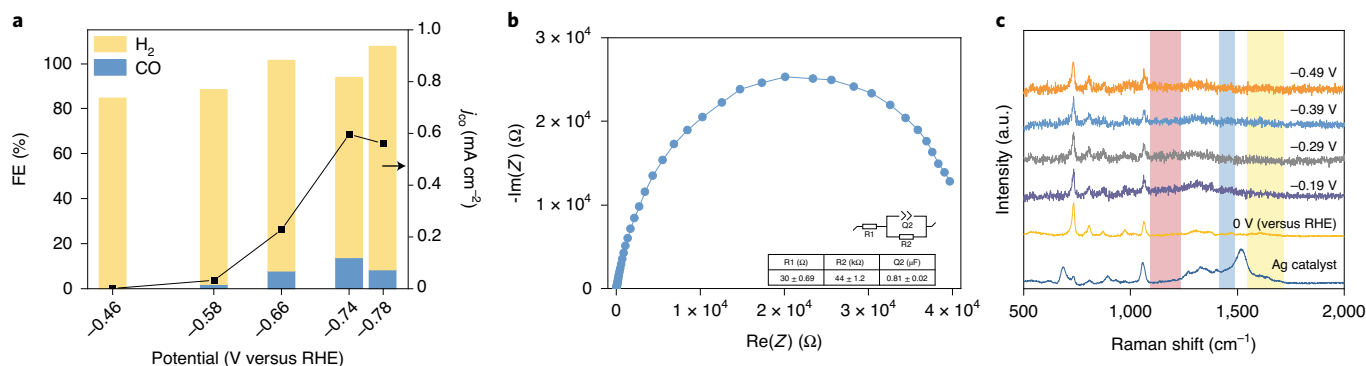


**Fig. 3 | The EDL in the case of the MEA/KCl electrolyte.** **a**, FE and partial current density of CO for the electrolyte of 2 M MEA with 2 M KCl and a Ag electrocatalyst. **b**, Impedance spectra for the MEA/KCl electrolyte collected at open circuit potential, approximately  $-0.145$  V versus Ag/AgCl. The inset is the equivalent circuit and the fit values of each components. R1 and R2 are the series resistance and charge transfer resistance, respectively; Q2 is the constant phase element. The error of each component denotes the standard deviation of three fit values from independent measurements. **c**, In situ surface-enhanced Raman spectroscopy for the MEA/KCl electrolyte.

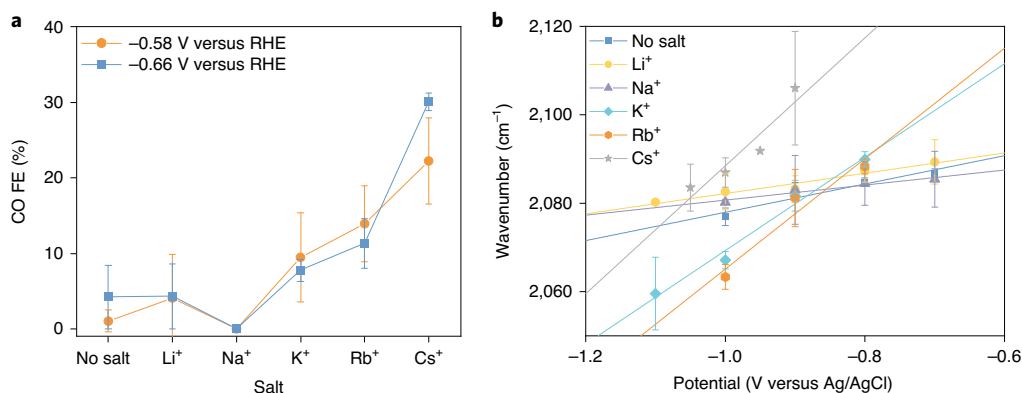


**Fig. 4 | The EDL tailored using different cations.** **a**, The FE for different alkali cation salt solutions in the MEA electrolyte at the applied potentials of  $-0.58$  V and  $-0.66$  V versus RHE. The error bars represent the standard deviation of measurements over three independent samples. **b**, Cation effects on the  $\text{CO}_{\text{ads}}$  stretching frequency shift at different applied potentials. The error bars indicate the standard deviation of the  $\text{CO}_{\text{ads}}$  frequency based on three independent measurements.

Furthermore, the slope of the frequency shift depends on the local electric field strength, which allows a direct reflection of the interfacial electric field with respect to the cationic species<sup>34,38,40</sup>:

$$\nu(\phi) = \nu_0 - \Delta\vec{\mu} \cdot \vec{E}(\phi) \quad (3)$$

where  $\nu(\phi)$  is the vibration frequency of the adsorbed CO at the applied potential ( $\phi$ ),  $\nu_0$  is the vibration frequency without an applied potential and  $\Delta\vec{\mu}$  is the field-free dipole moment known as the Stark tuning rate, which can be independently determined by experiment and simulation for a specific metal electrode and adsorbed molecules<sup>41,42</sup>.  $\vec{E}(\phi)$  is the potential-dependent interfacial electric field and the gradient of potential ( $\vec{E}(\phi) = -\nabla\phi$ ). Therefore, the slope of the frequency shift of  $\text{CO}_{\text{ads}}$  with respect to applied potential can be expressed as the derivative of electric field:

$$\frac{d\nu}{d\phi} = -\Delta\mu \frac{dE}{d\phi} \quad (4)$$

We can correlate this electric field strength with the thickness of the Helmholtz layer because the EDL is modelled as a parallel-plate capacitor in the Helmholtz model<sup>43</sup>.

**Table 1 | Electrochemical Stark tuning slopes from linearly fit lines with different cations**

Cation	MEA <sup>+</sup>	Li <sup>+</sup>	Na <sup>+</sup>	K <sup>+</sup>	Rb <sup>+</sup>	Cs <sup>+</sup>
Stark tuning slope ( $\text{V}^{-1}\text{cm}^{-1}$ )	$32 \pm 6$	$23 \pm 3$	$17 \pm 3$	$106 \pm 10$	$125 \pm 31$	$145 \pm 4$

The error bars correspond to the standard deviation of Stark tuning slopes from three independent measurements.

Figure 4b and Table 1 show the  $\text{CO}_{\text{ads}}$  frequency shift for the MEA electrolyte with and without alkali cations. The Stark tuning slopes for  $\text{K}^+$ ,  $\text{Rb}^+$  and  $\text{Cs}^+$  are significantly larger than those for  $\text{MEA}^+$ ,  $\text{Li}^+$  and  $\text{Na}^+$ , which agrees with the picture that the thickness of the electrochemical layer for  $\text{K}^+$ ,  $\text{Rb}^+$  and  $\text{Cs}^+$  is lower than that of  $\text{MEA}^+$ ,  $\text{Li}^+$  and  $\text{Na}^+$ . The agreement between the experimental results and proposed interfacial structure supports the contention that the introduction of different cations is capable of improving the electron transfer from the electrode to the chemisorbed  $\text{CO}_2$  and enables the direct electrolysis of amine- $\text{CO}_2$ .

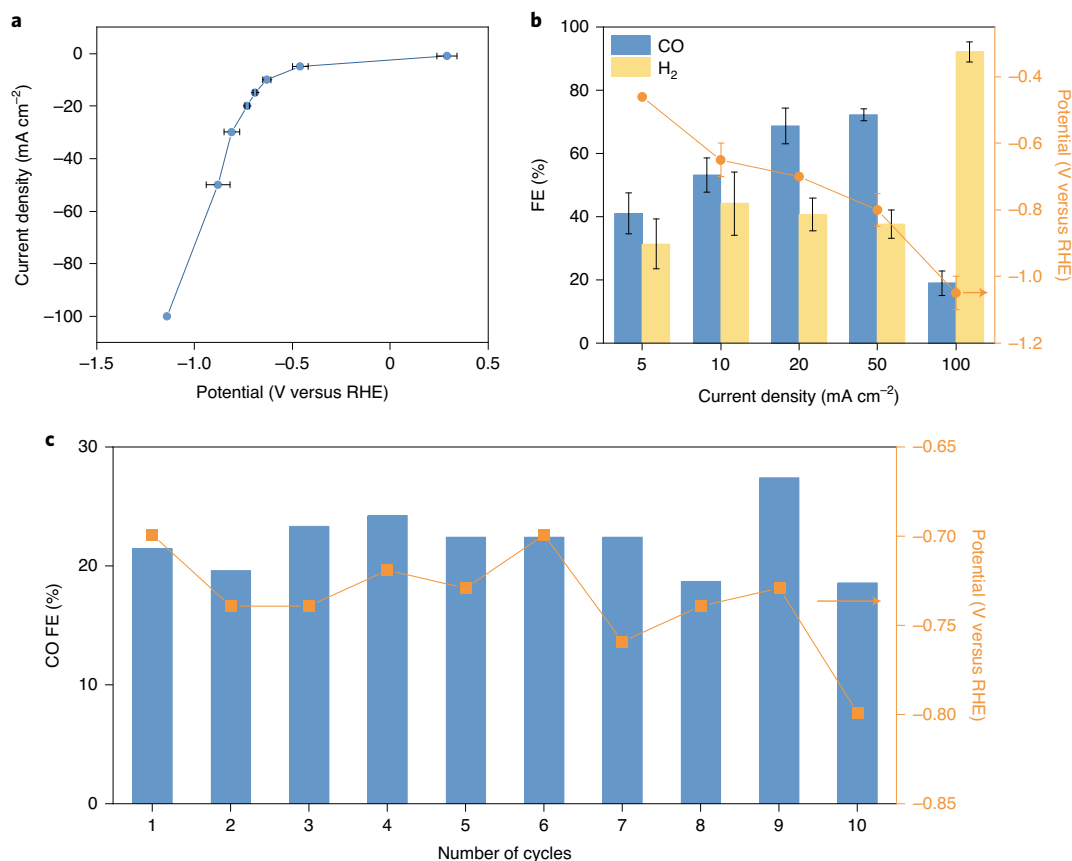


**Fig. 5 | Electrochemical performances of captured CO<sub>2</sub> electrolysis. a**, The current density versus potential curve at 60 °C for 30 wt% of MEA plus 70 wt% of H<sub>2</sub>O with 2 M KCl electrolyte in a flow cell system. The error bars represent the standard deviation of potentials from three independent measurements. **b**, Product distribution of MEA–CO<sub>2</sub> conversion to H<sub>2</sub> and CO at different applied current densities, ranging from 5 mA cm<sup>-2</sup> to 100 mA cm<sup>-2</sup> in a flow cell system. The error bars represent the standard deviation of three independent measurements. **c**, Recycling performance of the 2M MEA with 3M KCl electrolyte at a constant applied current density of 10 mA cm<sup>-2</sup> heated to 30 °C in a three-electrode configuration. Products were collected within 1h.

**Table 2 | Energy cost for an alkaline flow cell, gas-fed MEA cell, direct carbonate electrolysis and direct amine–CO<sub>2</sub> electrolysis**

System	Flow cell	MEA	Direct CO <sub>3</sub> <sup>2-</sup>	Direct amine–CO <sub>2</sub>
CO <sub>2</sub> utilization (%)	17	35	100	90
Carbonate formation (%)	45	0	0	10
Crossover (%)	2	30	0	0
Exit CO <sub>2</sub> (%)	36	35	0	0
CO <sub>2</sub> regeneration (kJ mol <sup>-1</sup> of product)	206	100	0	0
Electrolysis (kJ mol <sup>-1</sup> of product)	485	643	2,572	643
Product separation (kJ mol <sup>-1</sup> of product)	147	71	25	25
Total energy (kJ mol <sup>-1</sup> of product)	838	814	2,597	668
Total energy (kJ per tonne of product)	29	29	91	23

### Electrochemical regeneration of the amine capture solution

Because the reactant in this study is liquid amine–CO<sub>2</sub>, the gaseous products (CO and H<sub>2</sub>) are not diluted with unreacted CO<sub>2</sub> and offer a mixture of interest for the Fischer–Tropsch reaction. In order for electrolysis of amine–CO<sub>2</sub> to reach meaningful levels of utilization,

we sought to improve the current density and demonstrate the recyclability of the capture–electrolysis process. We heated the catholyte to ~40–80 °C to facilitate the breaking of the N–C bond. This temperature range is consistent with typical water electrolyser operating conditions and is significantly lower than the thermal regeneration temperature of an amine capture solution. The current density at 60 °C is 15 times higher than at room temperature. CO FE values increase with temperature as well (Supplementary Fig. 17). The increasing current density and the FE suggest that the products are generated from amine–CO<sub>2</sub> reactants, not dissolved CO<sub>2</sub>. The amount of dissolved CO<sub>2</sub> is limited by low solubility in an aqueous electrolyte; therefore, the current density is curtailed by mass transport<sup>44,45</sup>. The diffusion-limited current density for dissolved CO<sub>2</sub> was reported as ~10 mA cm<sup>-2</sup> under different testing conditions<sup>46–48</sup>. On the other hand, amine–CO<sub>2</sub> provides a concentration of ~2.5 M in this work<sup>49,50</sup>. The large current density serves as a qualitative indication that the reactant has to come from amine–CO<sub>2</sub>. In order to improve the electrochemical performance further, we implemented a Ag catalyst with added carbon black on polytetrafluoroethylene substrate to increase the local concentration of reactants<sup>51</sup>. We heated the catholyte, 30 wt% aqueous MEA solution with 2 M KCl, to 60 °C, and circulated the catholyte (electrochemical performances in the Methods section). Figure 5b shows the product distribution of CO and H<sub>2</sub> at different current density values ranging from 5 mA cm<sup>-2</sup> to 100 mA cm<sup>-2</sup>. The best CO FE is 72% at 50 mA cm<sup>-2</sup> and –0.8 V versus RHE. As shown in Fig. 5b, we achieve 100 mA cm<sup>-2</sup> current density with high CO FE. These

performance improvements are enabled by faster reactant transport and thermally assisted N–C bond cleavage.

To explore the recyclability of the electrolyte, we performed a cycling test of the amine–CO<sub>2</sub> electrolysis process. We first ran the amine–CO<sub>2</sub> electrolysis at a constant current density until the concentration of amine–CO<sub>2</sub> was depleted, a process that took ten hours of operation. A decrease in FE during the ten hour operation is observed and is explained by the depletion of the concentration of chemisorbed CO<sub>2</sub> (Supplementary Figs. 18 and 19). When the reaction ends, the electrolyte is re-purged with CO<sub>2</sub> and we then initiate a new cycle of electrolysis. The pH values of the electrolyte were measured at different stages of CO<sub>2</sub> purging and electrolysis (Supplementary Table 8): less than one pH unit of drift was observed. Figure 5c demonstrates the cycling performance of the electrolyte when electrolysis is run at a constant current density from the CO<sub>2</sub> capture electrolyte. We observed consistent CO FE in performance over ten continuous cycles. NMR spectra show the chemical structure of the carbamate after CO<sub>2</sub> purging and also the significant decrease of the carbamate signal at the end of a ten hour electrolysis (Supplementary Fig. 20). That electrolysis persisted for ten hours supports the contention that the reactant comes from amine–CO<sub>2</sub>, in light of its sufficient quantity.

### Energy analysis

To assess the prospects from a CO<sub>2</sub> reduction, we calculated the energy cost for different CO<sub>2</sub> reduction reaction systems and compared them to the amine–CO<sub>2</sub> system in this study. We compare alkaline flow cells<sup>52–55</sup>, gas-fed membrane electrode assembly cells<sup>56,57</sup>, direct carbonate electrolysis<sup>16</sup> and direct amine–CO<sub>2</sub> electrolysis. Table 2 summarizes the results; the details are in Supplementary Note 1 and Supplementary Tables 1–4. The total energy required to generate 1 mol of product from the direct chemisorbed CO<sub>2</sub> reduction system is comparable to the well-known CO<sub>2</sub> reduction reaction systems. We further estimated the dollar cost for the regeneration of carbonate and crossed-over CO<sub>2</sub> (Supplementary Note 2 and Supplementary Table 5). The economic analysis suggested that incomplete utilization will lead to a significant increase in total cost: this is in the range ~164 per tonne of product for both the MEA and flow cell systems studied in this example. This provides a sense of why amine–CO<sub>2</sub> systems are of interest: approaches that lever its ability to perform electrolysis directly from a capture liquid can reduce the energy cost (and carbon footprint) of the CO<sub>2</sub> capture process, as well as final product separation.

### Conclusion

We found that tuning the EDL enables the direct electrolysis of amine–CO<sub>2</sub> to value-added products, and does so in a way that allows recycling of the amine solvent. Electrochemical studies and in situ surface-enhanced Raman spectroscopy indicate that the adsorbed cations at the electrode surface influence electron transfer dynamics. We found that different constituents of the EDL can hinder or promote the heterogeneous electron transfer, a finding we attribute to the distance between the reactants and the electrode. With the aid of alkali cations, we achieve the direct electrolysis of the amine–CO<sub>2</sub> with 72% CO FE at 50 mA cm<sup>-2</sup>. The cyclability of the amine–CO<sub>2</sub> electrolyte was also demonstrated. The electrochemical strategy highlighted in this study offers a route to the design of CO<sub>2</sub> capture–electrolysis processes that will lower the energy cost and simplify the process flow.

### Methods

**Catalyst preparation.** All reagents used in this work were purchased from Sigma Aldrich without further purification. Ag catalysts were prepared by spray-coating Ag nanoparticle ink onto a sputtered Ag film. For the Ag film, Ag was sputtered on a carbon paper (AvCarb MGL190, Fuel Cell Store) using a Ag target at a sputtering rate of ~1 Å s<sup>-1</sup> to fabricate a 300-nm-thick Ag film. Ag nanoparticles (200 mg) were then dispersed in a mixture of 12.5 ml methanol and 400 µl Nafion and then

sonicated for 1 h. The Ag nanoparticle ink was spray-coated on the sputtered Ag with a loading of ~5 mg cm<sup>-2</sup> and dried under atmospheric conditions. The Ag catalysts were used for electrochemical characterization in an H-cell.

For flow cell systems, Ag and carbon black catalysts were prepared by spray-coating Ag nanoparticles with carbon black onto a sputtered Ag film. For the Ag film, Ag was sputtered on a polytetrafluoroethylene substrate (450 nm pore size) using a Ag target at a sputtering rate of ~1 Å s<sup>-1</sup> to fabricate a 300-nm-thick Ag film. Ag nanoparticles (200 mg) were dispersed in a mixture of 12.5 ml methanol, 400 µl Nafion and 50 mg carbon black (Super P Conductive, Alfa Aesar) and then sonicated for 1 h. The Ag/carbon-black nanoparticle ink was spray-coated on the sputtered Ag with a loading of ~5 mg cm<sup>-2</sup> and dried under atmospheric conditions.

**Electrochemical performance.** Electrochemical data were collected using an electrochemical station (PGSTAT204) in a three-electrode system and a flow cell system. All electrochemical data were collected under N<sub>2</sub> purging to remove dissolved CO<sub>2</sub> in the electrolyte. The as-prepared Ag catalyst was used as the working electrode in varying catholytes: 2 M aqueous solutions of MEA with or without supporting electrolyte. The anolyte was always a 1 M KOH solution. Pt foil and 3 M Ag/AgCl were used as the anode electrode and reference electrode, respectively. A Nafion 117 membrane was used to separate the two electrodes.

For the flow cell system, the as-prepared Ag/carbon-black catalyst was used as the working electrode in the catholyte: 30 wt% of MEA plus 70 wt% of H<sub>2</sub>O with 2 M KCl, and 2 M aqueous solutions of MEA with 2 M KCl. The anolyte was always a 1 M KOH solution. Ni foam and 3 M Ag/AgCl were used as the anode electrode and reference electrode, respectively. A Nafion 117 membrane was used to separate the cathode and the anode. The catholyte and anolyte were circulated using a peristaltic pump.

All potentials were applied against the Ag/AgCl reference electrode and then converted to the *iR*-corrected RHE scale using the following equation:

$$E_{\text{RHE}} = E_{\text{Ag/AgCl}} + 0.21 \text{ V} + 0.059 \times \text{pH} - iR$$

The series resistance of the system was determined by EIS.

The gas phase products were analysed using gas chromatography (PerkinElmer Clarus 580) equipped with a thermal conductivity detector and a flame ionization detector. All measurements were repeated three times to report the average and standard error.

EIS of the MEA and MEA/KCl electrolytes was conducted in the frequency range of 10<sup>5</sup> Hz to 0.01 Hz at the open circuit potential and at –0.4 V RHE, using a glassy carbon electrode as the working electrode, Pt foil as the counter electrode and Ag/AgCl as the reference electrode. The experiment was conducted in a three-electrode configuration without membrane separation. The EIS spectra were fitted with an equivalent circuit in the EC-Lab software.

Scan rate versus capacitive current data were obtained from cyclic voltammograms at the potential range from –0.2 V to 0.3 V versus Ag/AgCl in a three-cell electrode system, using a glassy carbon electrode as the working electrode, Pt foil as the counter electrode and Ag/AgCl as the reference electrode. The double-layer capacitance was determined from the slope of the non-Faradaic current versus scan rate graph.

**Characterization.** The morphology of the Ag catalyst was characterized by field emission scanning electron microscopy (Hitachi, SU5000); the X-ray diffraction (MiniFlex600) pattern was collected with Cu K $\alpha$  as the radiation source. Surface composition was analysed with ThermoFisher Scientific K-Alpha X-ray photoelectron spectroscopy using Al K $\alpha$  X-ray radiation. X-ray photoemission spectroscopy spectra were calibrated with the C 1s peak at 284.5 eV.

In situ surface-enhanced Raman spectroscopy was conducted with a Renishaw inVia Raman spectrometer using an in-house in situ cell and a  $\times 50$  water immersion lens. A Ag catalyst was used as the cathode in electrolytes of 2 M MEA or of 2 M MEA with 2 M KCl, purged with N<sub>2</sub> from the backside. Pt wire and Ag/AgCl were used as the anode and reference electrodes.

The Stark effect was characterized by in situ surface-enhanced Raman spectroscopy with a Renishaw inVia Raman spectrometer using an in-house in situ cell and a  $\times 50$  water immersion lens. A Cu catalyst was used as the cathode to collect the CO<sub>ad</sub> vibrational mode in different electrolytes purged with CO<sub>2</sub> from the backside. Pt wire and Ag/AgCl were used as the anode and reference electrodes, respectively. A 2 M aqueous solution of MEA with or without alkali salts was used as the electrolyte. Different potentials, from –0.7 V to –1.1 V versus Ag/AgCl, were held for 3 min before Raman experiments. All experiments were conducted by averaging three scans. Each scan shows the distinct CO vibrational signal between 2,000 cm<sup>-1</sup> and 2,100 cm<sup>-1</sup>, which can be ascribed to CO adsorption on the bridge and atop sites<sup>58–63</sup>. The bridge and atop-CO vibration signals sometimes overlap due to differences in the local environment in the different testing conditions<sup>59,63</sup>. Any signal with multiple peak shapes was deconvoluted to two different spectra for the bridged and atop binding configurations. The vibration frequency for the atop configuration was used for the Stark tuning slope analysis (Supplementary Fig. 16).

Chemical structures of the electrolytes were analysed with a 600 MHz Agilent DD2 <sup>1</sup>H NMR and <sup>13</sup>C NMR spectrometer. All NMR samples were prepared in D<sub>2</sub>O with a trimethylsilylpropanoic acid standard.

**CO<sub>2</sub> release.** First, 9 ml of 30 wt% aqueous MEA solution and 2 M aqueous KCl solution were prepared and saturated with CO<sub>2</sub>. A second solution with the same volume of 30 wt% MEA solution and 2 M KCl aqueous solution was prepared and saturated with CO<sub>2</sub> but was then re-purged with N<sub>2</sub> for 20 min to remove any dissolved CO<sub>2</sub>. Both solutions were heated at 70 °C for 15 min while collecting CO<sub>2</sub> release gas into a gas sampling bag. The volume of CO<sub>2</sub> release gas was measured by bubbling the gas to an inverted graduated cylinder. The difference in gas collected is attributed to the dissolved CO<sub>2</sub> in the electrolyte.

### Data availability

The authors declare that all data supporting the findings of this study are available within the paper and Supplementary Information files. Source data are provided with this paper.

Received: 2 April 2020; Accepted: 30 October 2020;

Published online: 07 December 2020

### References

1. Boot-Handford, M. E. et al. Carbon capture and storage update. *Energy Environ. Sci.* **7**, 130–189 (2014).
2. Wang, Y., Zhao, L., Otto, A., Robinius, M. & Stolten, D. A review of post-combustion CO<sub>2</sub> capture technologies from coal-fired power plants. *Energy Procedia* **114**, 650–665 (2017).
3. Haszeldine, R. S. Carbon capture and storage: how green can black be? *Science* **325**, 1647–1652 (2009).
4. Rheinhardt, J. H., Singh, P., Tarakeshwar, P. & Buttry, D. A. Electrochemical capture and release of carbon dioxide. *ACS Energy Lett.* **2**, 454–461 (2017).
5. Schmickler E. S. W. *Electrochemical Electron Transfer: from Marcus Theory to Electrocatalysis* (John Wiley and Sons, 2008).
6. Mizen, M. B. & Wrighton, M. S. Reductive addition of CO<sub>2</sub> to 9,10-phenanthrenequinone. *J. Electrochem. Soc.* **136**, 941–946 (1989).
7. Watkins, J. D. et al. Redox-mediated separation of carbon dioxide from flue gas. *Energy Fuels* **29**, 7508–7515 (2015).
8. Ranjan, R. et al. Reversible electrochemical trapping of carbon dioxide using 4,4'-bipyridine that does not require thermal activation. *J. Phys. Chem. Lett.* **6**, 4943–4946 (2015).
9. Singh, P. et al. Electrochemical capture and release of carbon dioxide using a disulfide–thiocarbonate redox cycle. *J. Am. Chem. Soc.* **139**, 1033–1036 (2017).
10. Appel, A. M., Newell, R., DuBois, D. L. & Rakowski DuBois, M. Concentration of carbon dioxide by electrochemically modulated complexation with a binuclear copper complex. *Inorg. Chem.* **44**, 3046–3056 (2005).
11. Stern, M. C. & Hatton, T. A. Bench-scale demonstration of CO<sub>2</sub> capture with electrochemically-mediated amine regeneration. *RSC Adv.* **4**, 5906–5914 (2014).
12. Stern, M. C., Simeon, F., Herzog, H. & Hatton, T. A. Post-combustion carbon dioxide capture using electrochemically mediated amine regeneration. *Energy Environ. Sci.* **6**, 2505–2517 (2013).
13. Chen, L. et al. Electrochemical reduction of carbon dioxide in a monoethanolamine capture medium. *ChemSusChem* **10**, 4109–4118 (2017).
14. Khurram, A., He, M. & Gallant, B. M. Tailoring the discharge reaction in Li–CO<sub>2</sub> batteries through incorporation of CO<sub>2</sub> capture chemistry. *Joule* **2**, 2649–2666 (2018).
15. Khurram, A., Yan, L., Yin, Y., Zhao, L. & Gallant, B. M. Promoting amine-activated electrochemical CO<sub>2</sub> conversion with alkali salts. *J. Phys. Chem. C* **123**, 18222–18231 (2019).
16. Li, Y. C. et al. CO<sub>2</sub> electroreduction from carbonate electrolyte. *ACS Energy Lett.* **4**, 1427–1431 (2019).
17. Wang, H., Yuan, X. Z. & Li, H. *PEM Fuel Cell Diagnostic Tools* (Taylor and Francis, 2011).
18. Ruffo, R. et al. Impedance analysis of Na<sub>0.44</sub>MnO<sub>2</sub> positive electrode for reversible sodium batteries in organic electrolyte. *Electrochim. Acta* **108**, 575–582 (2013).
19. Mizuno, Y. et al. Impedance spectroscopic study on interfacial ion transfers in cyanide-bridged coordination polymer electrode with organic electrolyte. *Electrochim. Acta* **63**, 139–145 (2012).
20. Baggetto, L., Niessen, R. A. H. & Notten, P. H. L. On the activation and charge transfer kinetics of evaporated silicon electrode/electrolyte interfaces. *Electrochim. Acta* **54**, 5937–5941 (2009).
21. Singh, R. K., Kunimatsu, K., Miyatake, K. & Tsuneda, T. Experimental and theoretical infrared spectroscopic study on hydrated Nafion membrane. *Macromolecules* **49**, 6621–6629 (2016).
22. Zeng, J., Jean, D.-I., Ji, C. & Zou, S. In situ surface-enhanced Raman spectroscopic studies of Nafion adsorption on Au and Pt electrodes. *Langmuir* **28**, 957–964 (2012).
23. Batista de Carvalho, L. A. E. & Teixeira-Dias, J. J. C. Raman spectra, conformational stability and normal coordinate analysis of ethylmethylamine. *J. Raman Spectrosc.* **26**, 653–661 (1995).
24. Long, D. A. Infrared and Raman characteristic group frequencies. *J. Raman Spectrosc.* **35**, 905–905 (2004).
25. Larkin P. *Infrared and Raman Spectroscopy: Principles and Spectral Interpretation* (Elsevier, 2011).
26. Tseng, C.-L., Chen, Y.-K., Wang, S.-H., Peng, Z.-W. & Lin, J.-L. 2-Ethanolamine on TiO<sub>2</sub> investigated by in situ infrared spectroscopy. Adsorption, photochemistry, and its interaction with CO<sub>2</sub>. *J. Phys. Chem. C* **114**, 11835–11843 (2010).
27. Geddes, A. L. & Bottger, G. L. Infrared spectra of silver-amine complexes. *Inorg. Chem.* **8**, 802–807 (1969).
28. Miles, M. G. et al. Raman and infrared spectra of isosteric diammine and dimethyl complexes of heavy metals. Normal-coordinate analysis of (X3Y2) 2Z ions and molecules. *Inorg. Chem.* **7**, 1721–1729 (1968).
29. Plotzker, I. & Exarhos, G. Spectroscopic studies of ammonia reduction of amorphous AgPO<sub>3</sub>. *J. Phys. Chem.* **84**, 3486–3486 (1980).
30. Gunathunge, C. M., Ovalle, V. J. & Waegele, M. M. Probing promoting effects of alkali cations on the reduction of CO at the aqueous electrolyte/copper interface. *Phys. Chem. Chem. Phys.* **19**, 30166–30172 (2017).
31. Strmcnik, D. et al. Effects of Li<sup>+</sup>, K<sup>+</sup>, and Ba<sup>2+</sup> cations on the ORR at model and high surface area Pt and Au surfaces in alkaline solutions. *J. Phys. Chem. Lett.* **2**, 2733–2736 (2011).
32. Thorson, M. R., Siil, K. I. & Kenis, P. J. A. Effect of cations on the electrochemical conversion of CO<sub>2</sub> to CO. *J. Electrochem. Soc.* **160**, F69–F74 (2013).
33. Resasco, J. et al. Promoter effects of alkali metal cations on the electrochemical reduction of carbon dioxide. *J. Am. Chem. Soc.* **139**, 11277–11287 (2017).
34. Li, J., Li, X., Gunathunge, C. M. & Waegele, M. M. Hydrogen bonding steers the product selectivity of electrocatalytic CO reduction. *Proc. Natl Acad. Sci. USA* **116**, 9220–9229 (2019).
35. McCrum, I. T., Hickner, M. A. & Janik, M. J. Quaternary ammonium cation specific adsorption on platinum electrodes: a combined experimental and density functional theory study. *J. Electrochem. Soc.* **165**, F114–F121 (2018).
36. Strmcnik, D. et al. The role of non-covalent interactions in electrocatalytic fuel-cell reactions on platinum. *Nat. Chem.* **1**, 466–472 (2009).
37. Pérez-Gallent, E., Marcandalli, G., Figueiredo, M. C., Calle-Vallejo, F. & Koper, M. T. M. Structure- and potential-dependent cation effects on CO reduction at copper single-crystal electrodes. *J. Am. Chem. Soc.* **139**, 16412–16419 (2017).
38. Ringe, S. et al. Understanding cation effects in electrochemical CO<sub>2</sub> reduction. *Energy Environ. Sci.* **12**, 3001–3014 (2019).
39. Singh, M. R., Kwon, Y., Lum, Y., Ager, J. W. & Bell, A. T. Hydrolysis of electrolyte cations enhances the electrochemical reduction of CO<sub>2</sub> over Ag and Cu. *J. Am. Chem. Soc.* **138**, 13006–13012 (2016).
40. Chattopadhyay, A. & Boxer, S. G. Vibrational Stark effect spectroscopy. *J. Am. Chem. Soc.* **117**, 1449–1450 (1995).
41. Bagus, P. S., Nelin, C. J., Müller, W., Philpott, M. R. & Seki, H. Field-induced vibrational frequency shifts of CO and CN chemisorbed on Cu(100). *Phys. Rev. Lett.* **58**, 559–562 (1987).
42. Ge, A. et al. Interfacial structure and electric field probed by *in situ* electrochemical vibrational Stark effect spectroscopy and computational modeling. *J. Phys. Chem. C* **121**, 18674–18682 (2017).
43. Bard, A. J. & Faulkner, L. R. *Electrochemical Methods: Fundamentals and Applications* 2nd edn (Wiley Textbooks, 2000).
44. Gupta, N., Gattrell, M. & MacDougall, B. Calculation for the cathode surface concentrations in the electrochemical reduction of CO<sub>2</sub> in KHCO<sub>3</sub> solutions. *J. Appl. Electrochem.* **36**, 161–172 (2006).
45. Zhong, H., Fujii, K., Nakano, Y. & Jin, F. Effect of CO<sub>2</sub> bubbling into aqueous solutions used for electrochemical reduction of CO<sub>2</sub> for energy conversion and storage. *J. Phys. Chem. C* **119**, 55–61 (2015).
46. Hatsukade, T., Kuhl, K. P., Cave, E. R., Abram, D. N. & Jaramillo, T. F. Insights into the electrocatalytic reduction of CO<sub>2</sub> on metallic silver surfaces. *Phys. Chem. Chem. Phys.* **16**, 13814–13819 (2014).
47. Rosen, J. et al. Mechanistic insights into the electrochemical reduction of CO<sub>2</sub> to CO on nanostructured Ag surfaces. *ACS Catal.* **5**, 4293–4299 (2015).
48. Singh, M. R., Clark, E. L. & Bell, A. T. Effects of electrolyte, catalyst, and membrane composition and operating conditions on the performance of solar-driven electrochemical reduction of carbon dioxide. *Phys. Chem. Chem. Phys.* **17**, 18924–18936 (2015).
49. Zhang, Y. et al. Rate-based process modeling study of CO<sub>2</sub> capture with aqueous monoethanolamine solution. *Ind. Eng. Chem. Res.* **48**, 9233–9246 (2009).
50. Lv, B., Guo, B., Zhou, Z. & Jing, G. Mechanisms of CO<sub>2</sub> capture into monoethanolamine solution with different CO<sub>2</sub> loading during the absorption/desorption processes. *Environ. Sci. Technol.* **49**, 10728–10735 (2015).
51. Zheng, T. et al. Large-scale and highly selective CO<sub>2</sub> electrocatalytic reduction on nickel single-atom catalyst. *Joule* **3**, 265–278 (2019).
52. Bhargava, S. S. et al. System design rules for intensifying the electrochemical reduction of CO<sub>2</sub> to CO on Ag nanoparticles. *ChemElectroChem* **7**, 2001–2011 (2020).

53. Dinh, C.-T. et al. CO<sub>2</sub> electroreduction to ethylene via hydroxide-mediated copper catalysis at an abrupt interface. *Science* **360**, 783–787 (2018).
54. Verma, S., Lu, X., Ma, S., Masel, R. I. & Kenis, P. J. A. The effect of electrolyte composition on the electroreduction of CO<sub>2</sub> to CO on Ag based gas diffusion electrodes. *Phys. Chem. Chem. Phys.* **18**, 7075–7084 (2016).
55. Verma, S. et al. Insights into the low overpotential electroreduction of CO<sub>2</sub> to CO on a supported gold catalyst in an alkaline flow electrolyzer. *ACS Energy Lett.* **3**, 193–198 (2018).
56. Jeong, H.-Y. et al. Achieving highly efficient CO<sub>2</sub> to CO electroreduction exceeding 300 mA cm<sup>-2</sup> with single-atom nickel electrocatalysts. *J. Mater. Chem. A* **7**, 10651–10661 (2019).
57. Li, Y. C. et al. Bipolar membranes inhibit product crossover in CO<sub>2</sub> electrolysis cells. *Adv. Sustain. Syst.* **2**, 1700187 (2018).
58. Dunwell, M., Wang, J., Yan, Y. & Xu, B. Surface enhanced spectroscopic investigations of adsorption of cations on electrochemical interfaces. *Phys. Chem. Chem. Phys.* **19**, 971–975 (2017).
59. Kudelski, A. & Pettinger, B. Fluctuations of surface-enhanced Raman spectra of CO adsorbed on gold substrates. *Chem. Phys. Lett.* **383**, 76–79 (2004).
60. Heyes, J., Dunwell, M. & Xu, B. CO<sub>2</sub> reduction on Cu at low overpotentials with surface-enhanced in situ spectroscopy. *J. Phys. Chem. C* **120**, 17334–17341 (2016).
61. Dederichs, F., Friedrich, K. A. & Daum, W. Sum-frequency vibrational spectroscopy of CO adsorption on Pt(111) and Pt(110) electrode surfaces in perchloric acid solution: effects of thin-layer electrolytes in spectroelectrochemistry. *J. Phys. Chem. B* **104**, 6626–6632 (2000).
62. Chernyshova, I. V., Somasundaran, P. & Ponnuram, S. On the origin of the elusive first intermediate of CO<sub>2</sub> electroreduction. *Proc. Natl Acad. Sci. USA* **115**, E9261–E9270 (2018).
63. Gunathunge, C. M. et al. Spectroscopic observation of reversible surface reconstruction of copper electrodes under CO<sub>2</sub> reduction. *J. Phys. Chem. C* **121**, 12337–12344 (2017).

## Acknowledgements

We acknowledge the support of the Ontario Research Fund and the Natural Sciences and Engineering Research Council (NSERC) of Canada. This research was supported by the Creative Materials Discovery Program through the National Research Foundation of Korea (NRF) funded by the Ministry of Science, ICT and Future Planning (2017M3D1A1040689).

## Author contributions

G.L. and Y.C.L. contributed to all experimental works, data analysis and manuscript preparation. J.-Y.K. and Y.-C.J. contributed to electrochemical experiments and NMR analysis. T.P. conducted the gas chromatography mass spectrometry analysis with the labelled <sup>13</sup>CO<sub>2</sub>. D.-H.N. and A.S.R. conducted catalyst characterization. F.L. and M.L. contributed to discussions of the mechanism. A.H.I. participated in discussion of the energy analysis. E.H.S. supervised this study.

## Competing interests

The authors declare no competing interests.

## Additional information

**Supplementary information** is available for this paper at <https://doi.org/10.1038/s41560-020-00735-z>.

**Correspondence and requests for materials** should be addressed to E.H.S.

**Peer review information** *Nature Energy* thanks Sichao Ma and the other, anonymous, reviewer(s) for their contribution to the peer review of this work.

**Reprints and permissions information** is available at [www.nature.com/reprints](http://www.nature.com/reprints).

**Publisher's note** Springer Nature remains neutral with regard to jurisdictional claims in published maps and institutional affiliations.

© The Author(s), under exclusive licence to Springer Nature Limited 2020